

Review



Cite this article: Morfu S, Usama BI, Marquié P. 2021 On some applications of vibrational resonance on noisy image perception: the role of the perturbation parameters. *Phil. Trans. R. Soc. A* **379**: 20200240.
<https://doi.org/10.1098/rsta.2020.0240>

Accepted: 23 October 2020

One contribution of 10 to a theme issue
'Vibrational and stochastic resonance in driven nonlinear systems (part 2)'.

Subject Areas:

computer vision, image processing,
sensory biophysics

Keywords:

vibrational resonance, image perception,
nonlinear stochastic dynamics

Author for correspondence:

S. Morfu
e-mail: smorfu@u-bourgogne.fr

On some applications of vibrational resonance on noisy image perception: the role of the perturbation parameters

S. Morfu, B. I. Usama and P. Marquié

ImViA EA 7535, Equipe Cores, Univ. Bourgogne Franche-Comté,
21000 Dijon, France

ID SM, 0000-0002-6436-4503

In this paper, we first propose a brief overview of nonlinear resonance applications in the context of image processing. Next, we introduce a threshold detector based on these resonance properties to investigate the perception of subthreshold noisy images. By considering a random perturbation, we revisit the well-known stochastic resonance (SR) detector whose best performances are achieved when the noise intensity is tuned to an optimal value. We then introduce a vibrational resonance detector by replacing the noisy perturbation with a spatial high-frequency signal. To enhance the image perception through this detector, it is shown that the noise level of the input images must be lower than the optimal noise value of the SR-based detector. Under these conditions, considering the same noise level for both detectors, we establish that the vibrational resonance (VR)-based detector significantly outperforms the SR-based detector in terms of image perception. Moreover, we show that whatever the perturbation amplitude, the best perception through the VR detector is ensured when the perturbation frequency exceeds the image size.

This article is part of the theme issue 'Vibrational and stochastic resonance in driven nonlinear systems (part 2)'.

1. Introduction

Over these past years, numerous studies have been devoted to the analyses of nonlinear systems and especially to their response to various stimulations. Indeed, nonlinear systems allow one to model phenomena which arise in nature, such as the behaviour of neurons,

transport mechanisms in living cells, climate dynamics, the behaviour of surface ocean, and so on. Depending on the driving of the nonlinear systems, different properties of resonance have been established with interesting applications in bioinspired information processing [1].

For instance, a nonlinear system, only excited with noise, can induce a response with a regularity which can be optimized for an optimal noise intensity. This effect, known as coherence resonance, has allowed the activity of neuron in absence of stimuli to be explained [2–4]. Besides this effect, stochastic resonance (SR) has been introduced as the ability of a nonlinear system to enhance its response to a stimuli for an optimal noise perturbation [5]. Neurons, such as mechanoreceptors of the crayfish, have revealed the possibility to use this effect to detect subthreshold stimuli. Moreover, it has been shown that SR also plays a crucial role in human visual perception [6]. Thus, different applications have been addressed ranging from signal detection and quantization [7–10] to image processing [11–13]. On the other hand, by mixing, through a nonlinear system, noise and a bi-chromatic excitation consisting of two frequencies, it has been also shown that a ghost frequency, lower than the weakest excitation frequencies, appears in the system response. This phenomenon, known as ghost stochastic resonance, has allowed to model pitch perception by the auditory system.

Lastly, it has been established that vibrational resonance (VR) occurs when a nonlinear system is driven by a low-frequency excitation perturbed by a high-frequency (HF) signal [14,15]. In fact, for an optimal value of the perturbation, the system enhances its response to the low-frequency excitation. Therefore, the detection of the low frequency by the nonlinear system is enhanced by the HF perturbation [16–18]. Similar to the SR effect, it is then not surprising that VR has been proved to occur in neurons models [19] and in neural networks [20,21], leading to applications in one-dimensional signal processing. However, contrary to SR applications [6,22], we must admit that very few studies have extended the applications of VR to two-dimensional signals [23–27], i.e. images [28]. In this paper, we propose to explore such applications in the image processing field. More precisely, we address the perception of subthreshold images through a VR-based detector. We first review some applications of nonlinear resonances in the field of image processing including visual perception. In this context, we then introduce a detector which can be based on stochastic or VRs. We also provide the general set-up of our study. Next, we highlight the limitations of SR in terms of image perception. In §5, we introduce a particular perturbation to show how VR can allow to overcome the limitation of SR. Unlike classical studies which usually consider the amplitude of the perturbation as a control parameter, we also analyse the impact of the frequency of the perturbation in terms of image perception. Section 6 is devoted to concluding remarks and outlooks.

2. Nonlinear resonance in the context of image processing, visual perception and dithering

(a) Image processing

As it is generally the case, the concept of image filtering with nonlinear resonances was first introduced with one-dimensional signals and is mainly based on the SR property: adding an appropriate amount of noise enhances the response of a system to a coherent information excitation. However, motivated by the fact that adding this optimal amount of noise in real system is not an easy task, parameter-induced stochastic resonance (PSR) has then been proposed as a convenient solution to take benefit of the noise enhanced property in the field of signal processing [29,30]. Later, the concept was extended to two-dimensional signals in the image processing field. In fact, the underlying strategy of PSR consists in changing the intrinsic characteristic of a nonlinear system to induce a cooperative effect between the input excitation and the noisy nonlinear system. In image processing, these techniques have revealed better results than a classical low-pass filter to denoise black and white images [31]. In fact, the measure of performance used in this study was the bit error ratio between the original noiseless image and

the processed image. A weaker error was observed for the PSR method which held more the image details at large noise intensity than when a simple low-pass filter was used.

Very recently, another way to take benefit of SR in image processing by adjusting the system parameters has been addressed in a nonlinear optical system containing photorefractive or nematic liquid crystals [32–35]. During this process of image enhancement, which uses modulation instability, the nonlinear coefficient of the crystal is controlled by an external voltage. For instance, Sun *et al.* have considered a nanosecond pulse signal carrying a high noisy image as the coherent information to be retrieved by this dynamical SR mechanism based on modulation instability [34]. While the noise intensity is constant, they have shown that an appropriate setting of the voltage controlling the nonlinearity allows one to extract with a fairly good efficiency the hidden image representing the number 20. The main advantage of their image recovery system is that it does not require any feedback or threshold, contrary to other SR-based methods. However, even if it does not dismiss the genuine interest of these works, we must admit that in such optical experiments, the considered images remain relatively basic. It is worth noting that optical image processing enhancement by noise has also been quantized earlier [36].

In the field of pattern recognition, by considering more complex images, such as those which represent fingerprints, potential applications of SR in biometric identification have been suggested [37]. For instance, by adding Gaussian noise with positive or negative mean value, whether an image pixel is in a dark or a bright region, Ryu *et al.* have computed a method based on SR which enhances the feature extraction of low-quality fingerprint images. Indeed, they have shown that, in a database where 20 fingerprints were rejected without image enhancement, SR succeeds in helping feature extraction from 10 of 11 weak contrasted fingerprints. Note that the nine remaining fingerprints of the database were damaged fingerprints for which all classical methods also failed to extract meaningful features. They have also shown that their SR-based method outperforms classical image enhancement processing such as histogram equalization. Indeed, their study reported that this classical method helps fingerprint detection for only five images among the 20 rejected of the database.

On the other hand, image contrast enhancement can also be achieved not by applying SR process directly to the grey levels of the image but rather indirectly in the Fourier domain [38,39]. Indeed, Chouhan *et al.* have proposed to let the Fourier coefficients of the image evolve in a double-well potential. After a given iterative numerical step, they reconstructed a filtered image by using an inverse Fourier transform. More precisely, they have shown that, for a given noisy image where the parameters of the potential can be tuned, there exists an optimal number of iterations for which the intrinsic image noise enhances the image contrast. In the context of medical image analysis, this indirect technique of noise improvement has also allowed to enhance magnetic resonance images as well as the enhancement of ultrasound images [40,41]. In this last case, a wavelet transform was used instead of the Fourier transform.

Other classical image processing algorithms have been modified to integrate the noise enhanced property. In the context of image denoising and edge preserving, we can cite the famous Perona & Malik process, based on the so-called diffusion equation which rules the heat transfer in its anisotropic form [42,43]. Histace & Rousseau have shown that including an optimal noise intensity inside the function which provides anisotropy allows one to restore images with better visual interest than those obtained with the classical Perona–Malik method [13,44]. Therefore, it is not surprising that noise enhanced image processing goes on to be widely investigated.

(b) Image perception

Image perception is another interesting field which has attracted a considerable attention since the early days of SR [6,45,46]. In their pioneering work, Simonotto *et al.* have reported that adding an appropriate amount of noise to a subthreshold image can enhance its perception through a simple threshold detector [6]. In fact, they have established that the perceptive contrast threshold of different subjects can be significantly reduced for an optimal noise level and that shorter noise correlation times provided the best enhancement. In their psychophysics experiments, noise

was spatially added to the subthreshold image and was not static but rather with temporal variations. By including such spatio-temporal random contributions, a basic model of a retina, which takes into account the random sampling by photoreceptors and the involuntary eye tremor [47], was next introduced and characterized by Zozor *et al.* [48]. They suggested that before encoding information in neurons, fluctuations may interfere in the first layer of the retina to acquire information on the whole image scene while tremors could perform an ensemble average. However, their study was restricted to the information acquisition by sensors and did not include the contribution of fluctuations in the neural process to account for the role of saccades in the transmission of the scene information by the higher layer of the retina. Nevertheless, they proved that noise can improve vision in their model at the acquisition process level. More recently, it has been shown that noise contributes to the perception of images consisting of alphabet characters by subjects with retinal disorder and impaired vision. More precisely, an optimal noise level added to images with contrast below the perceptible threshold has allowed the subjects to recognize better the letters than without noise [49]. However, in many studies devoted to visual perception, only the sensory receptors of the peripheral nervous system were taken into account since noise was directly mixed to the image stimuli. In other words, neural processing at the network level was almost neglected. Transcranial random noise stimulation (*tRNS*) of the cortex has then been introduced as a convenient solution to take into account such level of neural processing [50]. By performing a visual detection task to different subjects, it has been shown that exciting the visual cortex with *tRNS* enhances the detection of a specific stimuli, more precisely a sinusoidal luminance pattern within a Gaussian envelope in a circular aperture. In fact, the psychophysics experiments carried out by Van der Groen *et al.* consisted in finding in which of two separated sequences of images this specific visual stimuli had appeared. To analyse the influence of noise, they have estimated the percentage of correct responses in the cases where noise was directly added to the visual stimuli and when *tRNS* was used. Moreover, two different stimulations hypothesis were considered: subthreshold and suprathreshold stimuli. It was only under the subthreshold assumption that, for both noise cases, the detection performance exhibited a qualitative similar SR signature. Despite a better enhancement for noisy stimuli than with *tRNS*, their experiments have confirmed that under appropriate conditions, noise could improve perceptual decision-making. Impact of *tRNS* on visual stimuli perception is still currently under investigation to establish whether or not noise can enhance human behaviour [51].

(c) Nonlinear resonance and dithering

In the field of electronic and signal processing, the conversion from a continuous analogue signal to a digital one consists of a time discretization followed by an amplitude quantization which is similar to a multi-threshold filtering. Before quantization, an external perturbation, known as the dithering signal, is added to reduce the unavoidable loss of information and distortion occurring during signal quantization and mainly due to the error of quantization. It is therefore not surprising that SR and these dithering techniques have been described within the same scheme of noise induced threshold crossings [52]. However, some fundamental differences between these two processes have been widely discussed leading to the idea that SR and dithering are not mutually exclusive [10]. For instance, a copy of the dithering signal is often subtracted just after quantization, while it is not the case for processes based on nonlinear resonances. Even if dithering allows coding of amplitudes lower than the smallest quantizer threshold, dithering mainly affects suprathreshold signals, while SR enhances subthreshold signals.

On the other hand, dithering is also commonly applied to image processing and has found applications to LCD displays where it seems to have no universal dithering algorithms [53,54]. Nevertheless, among the dithering algorithms, random dithering, consisting in adding a noisy pattern to the initial image before quantization, is less efficient than ordered dithering, which uses coherent patterns [55]. Moreover, more complex algorithms, based on error propagation or which introduce spatio-temporal dependencies in the dithering patterns, provide better quantized

images. However, they cannot reduce to simple crossing threshold devices as they include propagative features.

Concerning applications of nonlinear resonances in image perception through threshold devices, we must admit that the subject has been restricted to SR where only random perturbations have been considered. Similar to dithering and noting that dithering and nonlinear resonances are not mutually exclusive, one may wonder if processes based on nonlinear resonances which use ordered perturbations, like VR, are more efficient in image perception than processes which use noisy perturbations, like SR. It constitutes the content of this paper since contrary to SR, the contribution of VR in image perception has not been yet clearly addressed. Indeed, in the following, we introduce a detector which uses perturbations whether random or ordered to better perceive different kinds of visual subthreshold stimuli, namely different images with various resolutions.

3. The detector and its set-up

(a) Input of the detector

To perform our study, we use the noiseless images of size $N \times N$ pixels represented in figure 1 and whose grey levels evolve from 0 (black) to 1 (white). As shown in figure 1, where the scales of the images have been respected, we propose different image sizes N^2 ranging from $N^2 = 64^2$ pixels to $N^2 = 512^2$ pixels. Each of these images I is then corrupted by an additive white noise of root mean square σ to generate the noisy image I_b according to

$$I_{b_{i,j}} = I_{i,j} + \sigma \eta_{i,j}, \quad \text{with } i = 1, 2, \dots, N \text{ and } j = 1, 2, \dots, N, \quad (3.1)$$

where $I_{i,j}$ denotes the grey level of the pixel of coordinates i, j and $\eta_{i,j}$ represents the unity Gaussian variance stochastic process with autocorrelation

$$\langle \eta_{i,j}, \eta_{i',j'} \rangle = \delta(i - i')\delta(j - j'). \quad (3.2)$$

Each of the obtained noisy images I_b is represented in figure 2 in the case considered throughout this paper, namely when the root mean square amplitude of the noise σ is set to $\sigma = 0.1$. For the sake of clarity, we have chosen to zoom each image which fits the same size without changing the image resolution N^2 which remains $N^2 = 64^2, N^2 = 128^2, N^2 = 256^2, N^2 = 512^2$ pixels for images 1, 2, 3 and 4, respectively.

These noisy images I_b , which can have different resolutions N^2 , will constitute the inputs of our resonant detector.

(b) The resonant threshold detector

The resonant detector, which is simulated in this paper, is described in figure 3. The noisy image input I_b of the threshold detector is first corrupted with an additive perturbation P which corresponds to noise in the case of a SR-based detector, while for a VR-based detector, P corresponds to an additive HF perturbation. Indeed, as shown in figure 3, a switch selects with a control c the appropriate perturbation between noise and HF sine spatial signal. The pixels grey levels $I_{P_{i,j}}$ of the perturbed image I_P are produced by adding the perturbation P to the noisy image I_b , thus they obey

$$I_{P_{i,j}} = P_{i,j} + I_{b_{i,j}}, \quad \text{with } i = 1, 2, \dots, N \text{ and } j = 1, 2, \dots, N. \quad (3.3)$$

More precisely, if we introduce c as a switch control which takes the Boolean value $c = 0$ for SR or $c = 1$ for VR, the perturbation added to each pixel of the noisy image I_b is defined by

$$P_{i,j} = c \times A \cos \left(\frac{2\pi ijN_{\text{HF}}}{N^2} + \varphi_{i,j} \right) + (1 - c) \times \gamma \eta'_{i,j} \quad \text{with } i = 1, 2, \dots, N \text{ and } j = 1, 2, \dots, N. \quad (3.4)$$



Figure 1. Images used throughout the paper with different sizes $N \times N$. Images 1, 2, 3 and 4 represent the Roman Colosseum, Saturn, a Cameraman and Lena. The resolution of images 1, 2, 3 and 4 are $N^2 = 64^2$ pixels, $N^2 = 128^2$ pixels, $N^2 = 256^2$ pixels and $N^2 = 512^2$ pixels, respectively.

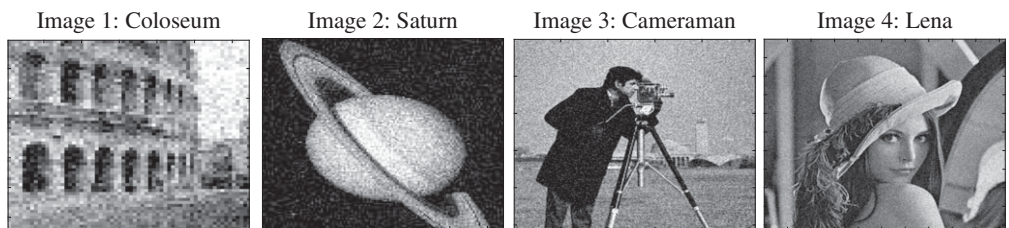


Figure 2. The noisy images I_b with noise intensity $\sigma = 0.1$. Each image has been zoomed even if they do not share the same resolution N^2 . Coloseum: $N^2 = 64^2$ pixels, Saturn: $N^2 = 128^2$ pixels, Cameraman: $N^2 = 256^2$ pixels, Lena: $N^2 = 512^2$ pixels.

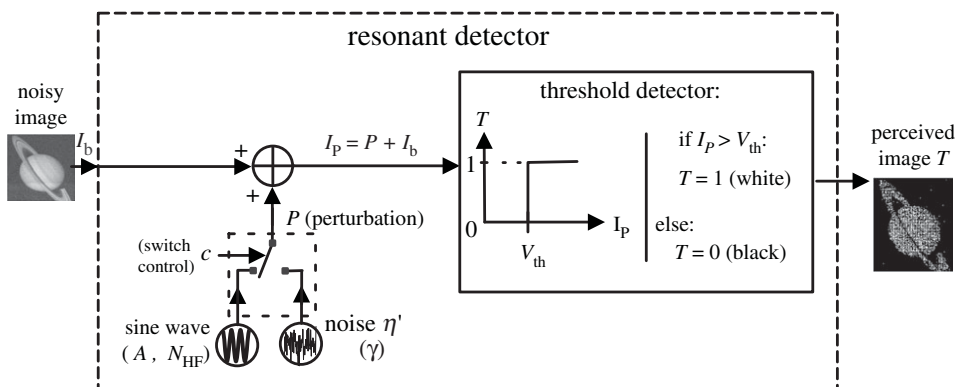


Figure 3. Sketch of the resonant detector which performs a threshold filtering of the perturbed image I_p and which perceives the black and white image T . The input of the resonant detector is the noisy image I_b which is perturbed by an additive perturbation P selected by a switch between noise or a sine perturbation. The switch command c chooses a noise perturbation η' of intensity γ in the case of a stochastic resonance-based detector, while for a vibrational resonance-based detector, a sine signal of amplitude A and spatial frequency N_{HF} is selected.

According to the value of the switch command c , the device which has been designed corresponds to:

- A SR-based detector (SR-detector) when $c = 0$. Indeed, in equation (3.4), the perturbation is the random term consisting of the unitary variance gaussian process η'_{ij} multiplied by the noise root mean square amplitude γ . In this case, the detector can be optimized by tuning the noise intensity γ of the perturbation.
- A VR-based detector (VR-detector) when the switch control is set to $c = 1$. In this case, the perturbation reduces to the HF cosine term of amplitude A , initial phase φ_{ij} and frequency adjusted with integer N_{HF} . In particular, the initial phase φ_{ij} is chosen randomly in a spatial gaussian distribution with standard deviation $\sigma_\varphi = 0.3\pi$, that is $\varphi_{ij} = \sigma_\varphi \zeta_{ij}$ where ζ_{ij} is a gaussian unitary variance process. Note that, in this paper, we propose to investigate how the detector can be optimized by tuning the perturbation parameters, namely its amplitude A but also its spatial frequency which is adjusted with N_{HF} .

In figure 3, the detector processes the perturbed image I_P to produce the output black and white image T by performing a threshold filtering with threshold V_{th} according to the following rules:

$$\begin{aligned} &\text{if } I_{P_{ij}} > V_{\text{th}}, T_{ij} = 1 \text{ (white level)} \\ &\text{else } T_{ij} = 0 \text{ (black level).} \end{aligned} \quad (3.5)$$

Moreover, the detector threshold used in equation (3.5) is chosen such that the unperturbed image I_b remains subthreshold, that is not detectable by the detector without the help of the perturbation P . For all the results presented in this article, to ensure this condition, we use $V_{\text{th}} = 1.2$. Lastly the performance of the detector is quantified by a measurement of similarity between the initial image I and the black and white detected image T . More precisely, we use the cross-covariance which constitutes a fairly appropriate measurement of similarity between two images [35,43,56]. This cross-covariance between image I and T is defined by

$$C_{I,T} = \frac{\langle (I - \langle I \rangle)(T - \langle T \rangle) \rangle}{\sqrt{\langle (I - \langle I \rangle)^2 \rangle \langle (T - \langle T \rangle)^2 \rangle}}, \quad (3.6)$$

where $\langle \cdot \rangle$ corresponds to an average over the whole image, that is an average across all the image pixels. Moreover, the cross-covariance defined by equation (3.6) was numerically estimated by an average over a sufficient number of realizations of the noisy process.

4. Stochastic resonance-based detector

The switch of the detector of figure 3 takes the value $c = 0$ such that the perturbation is a noise source of root mean square RMS amplitude γ . Therefore, in the case of a SR-detector, the perturbation defined by expression (3.4) reduces to

$$P_{ij} = \gamma \eta'_{ij} \text{ with } i = 1, 2, \dots, N \text{ and } j = 1, 2, \dots, N. \quad (4.1)$$

The black and white images T perceived by the detector are presented in figure 4 for growing values of the RMS amplitude of the noise perturbation, and in the case of the image 2 representing Saturn. For small noise intensities γ , as shown in figure 4a for $\gamma = 0.2$, threshold crossing events rarely occur. It results that they are not enough to allow the detector to retrieve the subthreshold information contained in the initial image. Next, for an intermediate value of the noise RMS amplitude, noise cooperates with the subthreshold image to reveal the coherent structure of the image. Indeed, the information is better perceived through the threshold detector for this optimal noise intensity $\gamma = 0.5$ in figure 4b. Lastly, for greater noise intensities, the random nature of noise dominates the process of threshold crossing and hinders the perception of the image information through the detector. The resulting image in figure 4c obtained for $\gamma = 1.2$ seems completely noisy.

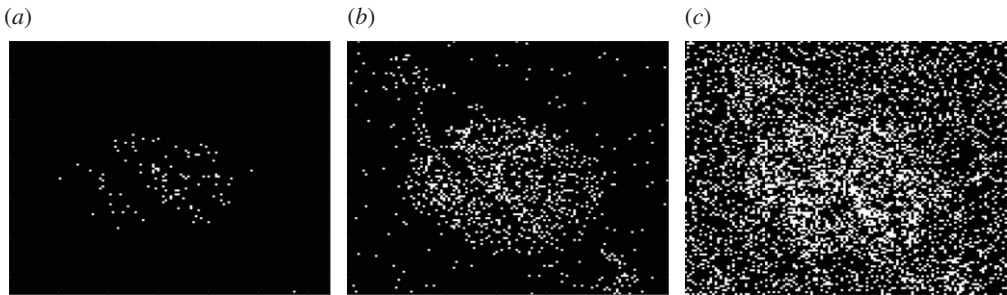


Figure 4. Images perceived by the SR-detector for different noise intensities γ . The initial noisy subthreshold image I_0 of Saturn is corrupted with the increasing noise RMS amplitude γ and threshold filtered with threshold $V_{\text{th}} = 1.2$ to produce the black and white images presented in subfigures (a–c). (a) $\gamma = 0.2$. (b) $\gamma = 0.5$. (c) $\gamma = 1.2$. The best perception of the Saturn image is obtained for the optimal noise value $\gamma^* = 0.5$ represented in subfigure (b).

This is a qualitative signature of SR, where an appropriate amount of noise enhances the response of a nonlinear system to a coherent input information. This effect is usually revealed by a quantitative performance measure of the system output which exhibits a resonance at an optimal RMS noise amplitude γ^* . The choice of the performance measure to highlight SR most often depends on the signal input and the context of applications. For instance, the signal to noise ratio is more appropriate for periodic signals, while for aperiodic signals the mutual information, the channel capacity, the probability of error [57–60] or the cross-covariance are rather preferred. In our case, we choose the cross-covariance C_{IT} defined by equation (3.6) since it is commonly used in the context of image processing [43,56] where images are rather aperiodic bidimensional signals. For the proposed image of Saturn, the cross-covariance C_{IT} is plotted with crosses against the noise level γ in figure 5a when the detector threshold V_{th} is set to $V_{\text{th}} = 1.2$. The curve exhibits a non-monotonous behaviour versus the noise intensity γ , which is a classical SR signature. Indeed, such a typical bell-shaped curve indicates that there exists an optimal value of the noise γ^* which optimizes the system response. Note that this optimal noise level γ^* is $\gamma^* = 0.5$, and also corresponds to the noise level used in figure 4b to obtain qualitatively the best image perception. Usually, the optimal performances of the system are strongly affected by the threshold of the detector. Especially, the gap between the subthreshold information signal and the threshold significantly affects the optimal performance that can be achieved by the system with the help of noise. To illustrate this feature, we have also plotted in figure 5a the cross-covariance for two other values of the threshold V_{th} , namely $V_{\text{th}} = 1.05$ plotted with circles and $V_{\text{th}} = 1.4$ plotted with diamonds. When the threshold is reduced, we observe that the optimal noise $\gamma^* = 0.4$ provides a better cross-covariance C_{IT} , while increasing the threshold to $V_{\text{th}} = 1.4$ involves a weaker cross-covariance. The curves presented for the three threshold values show that the more the image is far from the threshold, the less the perception of the image is of good quality. Moreover, in the same time, a greater noise level is required to optimize the system.

This fact can be visually confirmed if we compare the images perceived through the detector for each optimal noise intensity γ^* corresponding to each of the three considered thresholds, namely $\gamma^* = 0.4$ for $V_{\text{th}} = 1.05$, $\gamma^* = 0.5$ for $V_{\text{th}} = 1.2$ and $\gamma^* = 0.65$ for $V_{\text{th}} = 1.4$. These images are reported in figure 5b–d. It is clear that the best perception is achieved for the weakest threshold and that the quality of the perceived image decreases as the initial image is far from the threshold detector.

Note that in the whole article and in all that follows, we restrict our study to the intermediate value of the threshold $V_{\text{th}} = 1.2$.

We have also analysed the perception of the other initial images of figure 1 whose size N^2 ranges from $N^2 = 64^2$ pixels to $N^2 = 512^2$ pixels. Our results are summarized in figure 6. For all the considered initial images, a SR type curve is observed for the evolution of the cross-covariance against the RMS noise level γ . Moreover, for each of the initial images of figure 1, we propose in

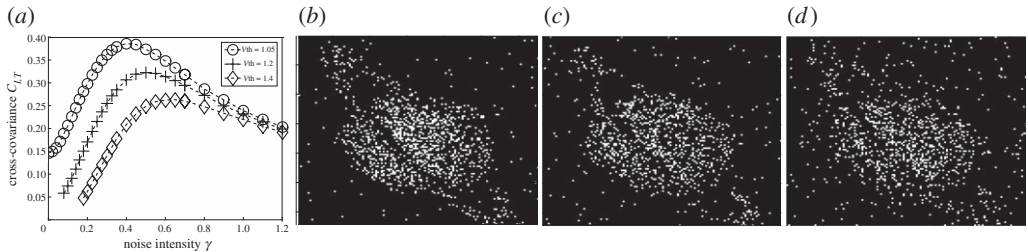


Figure 5. Perception of the Saturn image through the SR-detector for different threshold levels V_{th} . Parameter: $\sigma = 0.1$. (a) Cross-covariance $C_{l,T}$ versus the noise intensity γ for three different threshold values V_{th} . Dashed lines are guides to the eye. The best perceived images obtained for the optimal noise intensity γ^* are displayed for each considered threshold value V_{th} in subfigures (b–d). (b) $V_{th} = 1.05$ requires $\gamma^* = 0.4$ to achieve $C_{l,T}(\gamma^*) = 0.386$. (c) $V_{th} = 1.2$ requires $\gamma^* = 0.5$ to achieve $C_{l,T}(\gamma^*) = 0.322$. (d) $V_{th} = 1.4$ requires $\gamma^* = 0.65$ to achieve $C_{l,T}(\gamma^*) = 0.263$.

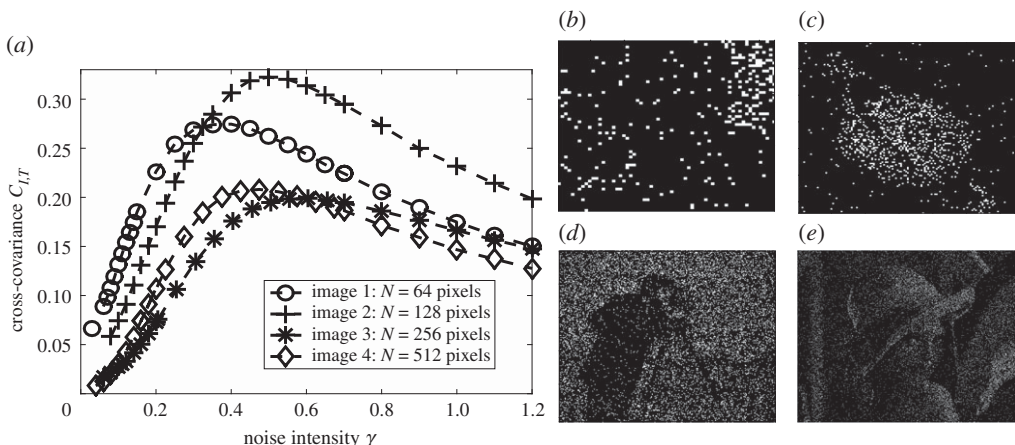


Figure 6. Perception of the different images through the SR-detector. Parameters: $V_{th} = 1.2$ and $\sigma = 0.1$. (a) Cross-covariance $C_{l,T}$ of each image against the noise intensity γ . Dashed lines are guides to the eye. The best perceived images are displayed for the optimal noise intensity γ^* in subfigures (b–d). (b) image 1 requires $\gamma^* = 0.39$ to achieve $C_{l,T}(\gamma^*) = 0.274$. (c) Image 2 requires $\gamma^* = 0.5$ to achieve $C_{l,T}(\gamma^*) = 0.322$. (d) Image 3 requires $\gamma^* = 0.59$ to achieve $C_{l,T}(\gamma^*) = 0.199$. (e) Image 4 requires $\gamma^* = 0.465$ to achieve $C_{l,T}(\gamma^*) = 0.208$.

figure 6b–d the best image perceived when the noise intensity is tuned to the noise level γ^* which maximizes the cross-covariance. Except for the first image of the Coloseum, SR reveals quite fairly the information contained in each subthreshold initial image. In fact, the effect is less pronounced for the image of the Coloseum owing to its very low resolution of $N^2 = 64^2$ pixels, which is not the most appropriate resolution to observe image details. Note that we have reported in table 1 all the necessary features of our SR-detector, that is for each initial image the image size, the optimal noise intensity γ^* and the best value of the cross-covariance $C_{l,T}$ achieved for $\gamma = \gamma^*$. These values will be of crucial interest to develop the VR-detectors presented in the next section.

5. Vibrational resonance-based detector

By setting the switch control c of the detector to $c = 1$, the perturbation P of figure 3 defined by equation (3.4) takes the form of the following sine function:

$$P_{i,j} = A \cos \left(\frac{2\pi ijN_{HF}}{N^2} + \varphi_{i,j} \right) \text{ with } i = 1, 2, \dots, N \text{ and } j = 1, 2, \dots, N. \quad (5.1)$$

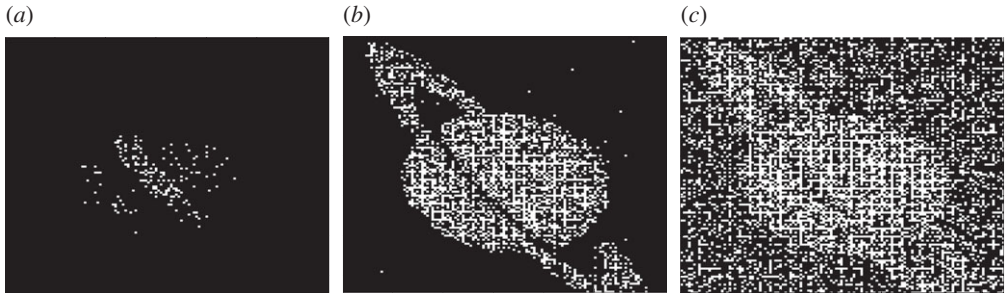


Figure 7. Images perceived by the VR-detector for different perturbation amplitudes A . The initial noisy subthreshold image I_0 of Saturn is corrupted with increasing perturbation amplitude A and then threshold filtered with threshold $V_{\text{th}} = 1.2$ to produce the black and white images presented in subfigures (a–c). (a) $A = 0.3$. (b) $A = 0.95$. (c) $A = 1.4$. The best perception of Saturn image is obtained for the optimal perturbation amplitude $A = 0.95$ in subfigure (b).

Table 1. Features of the stochastic resonance-based detector with threshold $V_{\text{th}} = 1.2$. γ^* represents the optimal noise intensity which maximizes the cross-covariance $C_{I,T}$.

| image number | image size N^2 | optimal noise γ^* | best cross-covariance $C_{I,T}(\gamma = \gamma^*)$ |
|--------------------|---------------------|-----------------------------|---|
| Image 1: Coloseum | 64^2 | 0.39 | 0.274 |
| Image 2: Saturn | 128^2 | 0.5 | 0.322 |
| Image 3: Cameraman | 256^2 | 0.59 | 0.199 |
| Image 4: Lena | 512^2 | 0.465 | 0.208 |

In this section, we analyse how the perception of the images presented in figure 1 through the VR-detector can be optimized by tuning the perturbation amplitude A and its spatial frequency N_{HF} . Therefore, it leads us to first define an amplitude optimized VR-detector obtained when the frequency N_{HF} of the perturbation remains constant while its amplitude A can be adjusted. Next, motivated by the work of Yao *et al.* [61], who have obtained better resonances when the perturbation frequency can be tuned, we propose to develop a frequency optimized VR-detector: the amplitude of the perturbation will remain constant while its frequency will be adjusted.

(a) Amplitude optimized VR-detector

For each image of figure 1, the spatial frequency N_{HF} of the perturbation is adjusted according to the image resolution N^2 to ensure that the normalized frequency N_{HF}/N^2 remains constant, while the perturbation amplitude A can be tuned. We arbitrarily choose the normalized value $N_{\text{HF}}/N^2 = 1/4$ which is not restrictive since the influence of the normalized frequency will be addressed in the next subsection. Like the SR-detector, we first consider the noisy image of Saturn whose resolution is $N^2 = 2^{14}$ pixels and whose level of noise is $\sigma = 0.1$. It means that in this case, the frequency of the perturbation must be tuned to $N_{\text{HF}} = 2^{12}$ to ensure $N_{\text{HF}}/N^2 = 1/4$.

Figure 7 displays the different images perceived by the detector for growing values of the perturbation amplitude A .

For the weakest perturbation amplitude, namely $A = 0.3$, the threshold triggerings induced by the addition of perturbation are not sufficient to enable the perception of the initial image with a good quality.

However, in the case of figure 7b, for the intermediate amplitude value $A = 0.95$, the perturbation positively helps the initial subthreshold image to cross the threshold. The perception of the initial image details is then the best and qualitatively exceeds the quality reported with

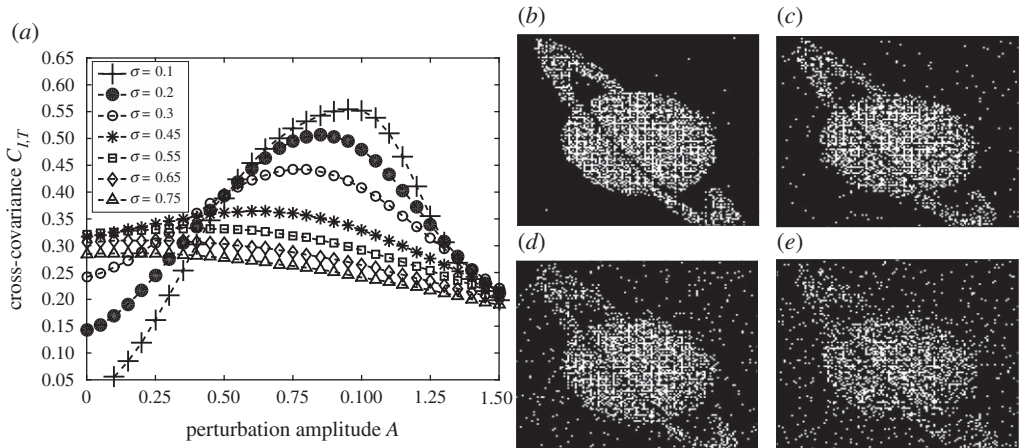


Figure 8. Perception through the VR-detector of the Saturn image with different noise intensities σ . Parameter: $V_{\text{th}} = 1.2$. (a) Cross-covariance $C_{I,T}$ against the perturbation amplitude A for different levels of noise σ . Dashed lines are guides to the eye. For each noise intensity σ where a resonance of the cross-covariance occurs, we have displayed the best perceived image obtained for the optimal perturbation amplitude A^* in subfigures (b–e). (b) $\sigma = 0.1$ requires $A^* = 0.95$ to achieve $C_{I,T}(A^*) = 0.554$. (c) $\sigma = 0.2$ requires $A^* = 0.85$ to achieve $C_{I,T}(A^*) = 0.506$. (d) $\sigma = 0.3$ requires $A^* = 0.8$ to achieve $C_{I,T}(A^*) = 0.442$. (e) $\sigma = 0.45$ requires $A^* = 0.6$ to achieve $C_{I,T}(A^*) = 0.365$.

the SR-detector in figure 4*b*. By contrast, for the greatest perturbation amplitude considered in figure 7*c*, the information contained in the initial image is not well retrieved by the detector because the threshold triggerings are ruled rather by the perturbation than by the initial image. It results that the perceived image is dominated by the HF perturbation. To quantify the performance of the VR-detector, we have plotted in figure 8*a* the cross-covariance $C_{I,T}$ against the perturbation amplitude A for different levels of noise σ ranging from $\sigma = 0.1$ to $\sigma = 0.75$. First, to compare the VR-detector and the SR-detector, it is necessary to consider the same level of noise in the input initial image I_b for both detectors. Therefore, since we used a noise level $\sigma = 0.1$ for the SR-detector, we can first comment on the curve plotted with crosses in figure 8*a* which corresponds to the same noise intensity $\sigma = 0.1$. This curve, which shows the evolution of the cross-covariance $C_{I,T}$ versus the perturbation amplitude A , presents non-monotonous behaviour with a maximum value $C_{I,T} = 0.554$ achieved for a perturbation amplitude $A^* = 0.95$. Such resonance curve constitutes the classical signature of the VR phenomenon. Moreover, the optimal value of the cross-covariance exceeds the one obtained with the SR-detector which was $C_{I,T} = 0.322$ for the same noisy Saturn image. It quantitatively confirms that VR-detector perceives noisy images with a better quality than SR-detectors. The same resonant behaviours of the cross-covariance are reported in figure 8*a* for the noise intensity $\sigma = 0.2$ (filled circles), $\sigma = 0.3$ (empty circles) and $\sigma = 0.45$ (stars). The corresponding optimal images are proposed in figure 8*c–e* respectively. In addition, we recall in figure 8*b* the optimal image obtained with the VR-detector when the noise level is $\sigma = 0.1$. We observe that the quality of the perceived image decreases as the noise level of the initial image increases. In fact, it is not surprising since the maxima of the cross-covariance also reduces with increasing values of noise in figure 8*a*.

On the other hand, figure 8*a* also reveals that VR ceases to exist when the noise level σ of the initial image exceeds the optimal noise RMS value γ^* of the SR-detector. Indeed, the cross-covariance is a monotonous decreasing function of the perturbation amplitude for the noise intensity $\sigma = 0.55$ (squares), $\sigma = 0.65$ (diamonds) and $\sigma = 0.75$ (triangles) which are beyond the critical noise value $\gamma^* = 0.5$. The result is that there exists a critical value of noise beyond which no perception enhancement can be expected with VR.

We also propose to analyse if the image resolution N^2 impacts the performances of the VR-detector. Therefore, we consider the other images of figure 1 with the same level of

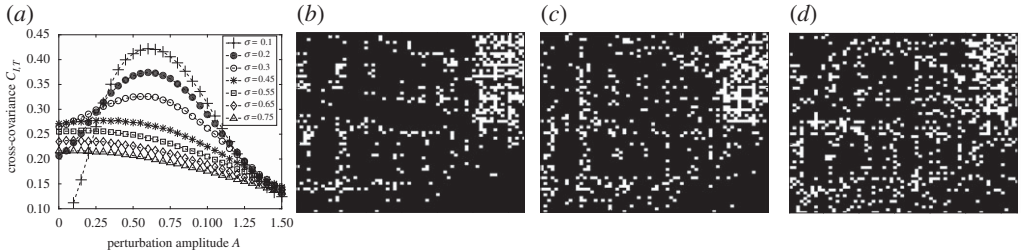


Figure 9. Perception through the VR-detector of the Coloseum image with different noise intensities σ . Parameter: $V_{\text{th}} = 1.2$. (a) Cross-covariance $C_{I,T}$ against the perturbation amplitude A for different levels of noise σ . Dashed lines are guides to the eye. For each noise intensity σ where a resonance of the cross-covariance occurs, we have displayed the best perceived image obtained for the optimal perturbation amplitude A^* in subfigures (b–d). (b) $\sigma = 0.1$ requires $A^* = 0.6$ to achieve $C_{I,T}(A^*) = 0.422$. (c) $\sigma = 0.2$ requires $A^* = 0.6$ to achieve $C_{I,T}(A^*) = 0.374$. (d) $\sigma = 0.3$ requires $A^* = 0.6$ to achieve $C_{I,T}(A^*) = 0.325$.

noise ranging from $\sigma = 0.1$ to $\sigma = 0.75$. The cross-covariances have been estimated against the amplitude of the perturbation A , while the spatial normalized perturbation frequency remains $N_{\text{HF}}/N^2 = 1/4$. Our results for the first image representing the Coloseum are reported in figure 9 with $N_{\text{HF}} = 2^{10}$ since $N^2 = 2^{12}$. First, we recall from table 1 that the optimal noise value γ^* which maximized the SR-detector was $\gamma^* = 0.39$ with a maximal value of the cross-covariance $C_{I,T}(\gamma^*) = 0.274$. Figure 9a confirms that VR ceases to exist for noise intensities σ exceeding γ^* . Indeed, only the curves corresponding to the noise levels $\sigma = 0.1$, $\sigma = 0.2$ and $\sigma = 0.3$ exhibit a resonant behaviour, while for the other noise values, namely $\sigma = 0.45$, $\sigma = 0.55$, $\sigma = 0.65$, $\sigma = 0.75$, the cross-covariance $C_{I,T}$ monotonously decreases against the perturbation amplitude A . Nevertheless, for the noise intensity $\sigma = 0.1$, the VR-detector perceives the initial image better than the SR-detector since a cross-covariance $C_{I,T} = 0.422$ is reached for the optimal perturbation amplitude $A^* = 0.6$. Comparing figures 6b and 9b, which display the perceived image through each detector, there is no doubt that the VR-detector outperforms the SR-detector. However, when the noise level of the initial image increases in figure 9c,d, the quality of the retrieved image reduces.

The results obtained with the third image representing the Cameraman with a resolution of $N^2 = 256^2$ pixels are available in figure 10. Note that the perturbation frequency is now tuned to $N_{\text{HF}} = 2^{14}$ to satisfy the condition $N_{\text{HF}}/N^2 = 1/4$. According to table 1, VR is expected to occur for noise levels σ below the critical value $\gamma^* = 0.59$. It is verified in figure 10a, where the evolution of the cross-covariance versus the perturbation amplitude exhibits a resonance only for the noise intensities $\sigma = 0.1$, $\sigma = 0.2$, $\sigma = 0.3$, $\sigma = 0.45$ and $\sigma = 0.55$. Note that in the later case, the resonance is less pronounced since the noise level $\sigma = 0.55$ is close to the critical value $\gamma^* = 0.59$. The corresponding images perceived through the VR-detector are also presented in figure 10b–e to provide a qualitative overview of the optimal achieved performances according to the noise level.

Lastly, the fourth image representing Lena with a resolution of $N^2 = 512^2$ pixels is used as the subthreshold image input. It leads one to consider a spatial perturbation frequency $N_{\text{HF}} = 2^{16}$ since we fit the condition $N_{\text{HF}}/N^2 = 1/4$. Once again, the cross-covariance $C_{I,T}$ can be maximized for an optimal amplitude A^* of the HF perturbation if the noise level of the input image σ remains below the critical noise value γ^* defined by the SR-detector. For the image of Lena, we have established in table 1 that this critical value is $\gamma^* = 0.465$. Therefore, the curves of cross-covariance, which correspond to the noise intensities $\sigma = 0.1$, $\sigma = 0.2$, $\sigma = 0.3$ and $\sigma = 0.45$, exhibit a behaviour with a resonance in figure 11a. It indicates that an appropriate tuning of the perturbation amplitude to A^* allows to enhance the perception of the subthreshold noisy image to be enhanced. The perceived images for each noise level are reported in figure 11b–e when the perturbation amplitude has been optimally set to A^* . In particular, the perceived image of figure 11b can be compared with the one obtained with the SR-detector in figure 6e since they share the same input noise level $\sigma = 0.1$. It is clearly established that, whatever the

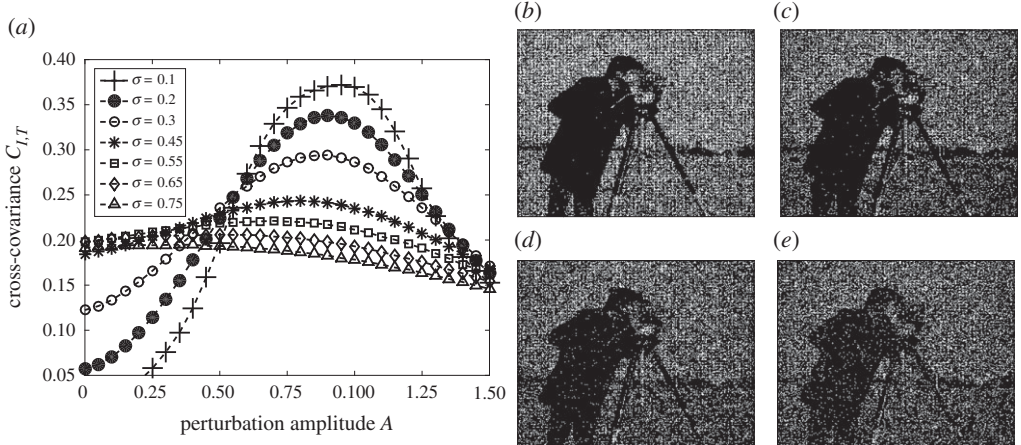


Figure 10. Perception through the VR-detector of the Cameraman image with different noise intensities σ . Parameter: $V_{\text{th}} = 1.2$. (a) Cross-covariance $C_{I,T}$ against the perturbation amplitude A for different levels of noise σ . Dashed lines are guides to the eye. For each noise intensity σ where a resonance of the cross-covariance occurs, we have displayed the best perceived image obtained for the optimal perturbation amplitude A^* in subfigures (b–e). (b) $\sigma = 0.1$ requires $A^* = 0.95$ to achieve $C_{I,T}(A^*) = 0.372$. (c) $\sigma = 0.2$ requires $A^* = 0.9$ to achieve $C_{I,T}(A^*) = 0.342$. (d) $\sigma = 0.3$ requires $A^* = 0.9$ to achieve $C_{I,T}(A^*) = 0.292$. (e) $\sigma = 0.45$ requires $A^* = 0.8$ to achieve $C_{I,T} = 0.243$.

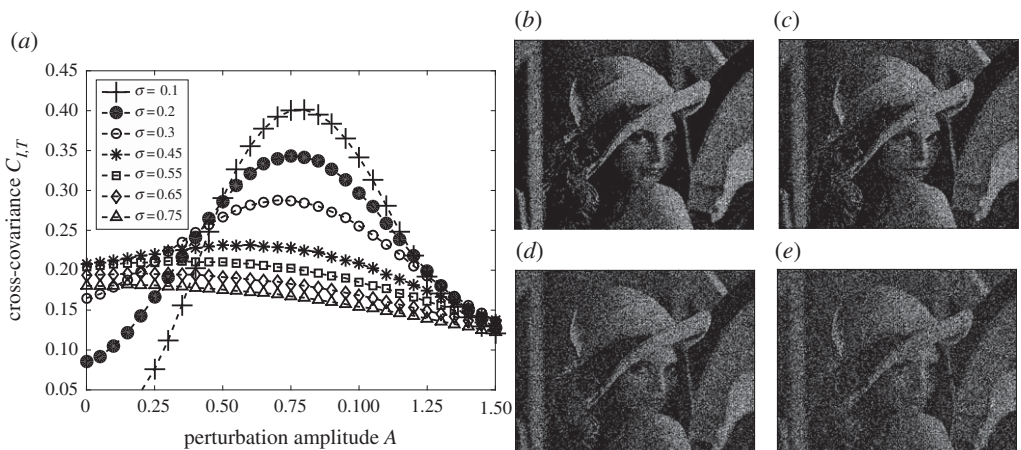


Figure 11. Perception through the VR-detector of the Lena image with different noise intensities σ . Parameter: $V_{\text{th}} = 1.2$. (a) Cross-covariance $C_{I,T}$ against the perturbation amplitude A for different levels of noise σ . Dashed lines are guides to the eye. For each noise intensity σ where a resonance of the cross-covariance occurs, we have displayed the best perceived image obtained for the optimal perturbation amplitude A^* in subfigures (b–e). (b) $\sigma = 0.1$ requires $A^* = 0.8$ to achieve $C_{I,T}(A^*) = 0.401$. (c) $\sigma = 0.2$ requires $A^* = 0.75$ to achieve $C_{I,T}(A^*) = 0.343$. (d) $\sigma = 0.3$ requires $A^* = 0.7$ to achieve $C_{I,T}(A^*) = 0.288$. (e) $\sigma = 0.45$ requires $A^* = 0.6$ to achieve $C_{I,T}(A^*) = 0.232$.

considered image, a better enhancement of image perception is achieved with the VR-detector than with the SR-detector. By contrast, the cross-covariance monotonously decreases for noise intensities $\sigma = 0.55$, $\sigma = 0.65$ and $\sigma = 0.75$, revealing that no enhancement of perception through the VR-detector can be obtained if the noise of the input image exceeds the critical value γ^* .

The main features of the VR-detector are summarized in table 2 when the normalized spatial frequency of the perturbation remains $N_{\text{HF}}/N^2 = 1/4$. First, we have specified the critical noise

Table 2. Features of the VR-detector with spatial normalized frequency $N_{HF}/N^2 = 1/4$ and threshold $V_{th} = 1.2$. A^* represents the optimal amplitude of the perturbation which maximizes the cross-covariance $C_{I,T}$ and γ^* the critical noise value beyond which the detector cannot recover the subthreshold image.

| image number | critical noise γ^* | $C_{I,T}(A^*)$ for $\sigma = 0.1$ | $C_{I,T}(A^*)$ for $\sigma = 0.2$ | $C_{I,T}(A^*)$ for $\sigma = 0.3$ |
|-----------------------------|---------------------------|-----------------------------------|-----------------------------------|-----------------------------------|
| 1: Coloseum $N^2 = 2^{12}$ | 0.39 | 0.422 for $A^* = 0.6$ | 0.374 for $A^* = 0.6$ | 0.325 for $A^* = 0.6$ |
| 2: Saturn $N^2 = 2^{14}$ | 0.5 | 0.554 for $A^* = 0.95$ | 0.506 for $A^* = 0.85$ | 0.442 for $A^* = 0.8$ |
| 3: Cameraman $N^2 = 2^{16}$ | 0.59 | 0.372 for $A^* = 0.95$ | 0.342 for $A^* = 0.9$ | 0.292 for $A^* = 0.9$ |
| 4: Lena $N^2 = 2^{18}$ | 0.465 | 0.401 for $A^* = 0.8$ | 0.343 for $A^* = 0.75$ | 0.288 for $A^* = 0.7$ |

level γ^* beyond which the detector fails to enhance image perception. Next, for each noise intensity σ below γ^* , we provide the value A^* of the perturbation amplitude which gives the best image perception and the corresponding maximum value of the cross-covariance $C_{I,T}(A^*)$. This table shows that as the noise intensity increases, the performance of the VR reduces, whatever the considered images. Moreover, except for the first image of the Coloseum whose resolution N is very poor, it requires a weaker amplitude of the perturbation A^* for greater noise intensity to achieve the best performance. One may wonder if the normalized spatial frequency N_{HF}/N^2 of the perturbation would have an impact on the performances achieved by the detector. It is the aim of the next subsection for which table 2 will constitute a reference.

(b) Frequency optimized VR-detector

We now consider that the spatial normalized frequency N_{HF}/N^2 of the perturbation evolves, while the amplitude of the perturbation A remains constant. Our study concerning the effect of the perturbation frequency has been carried out for the five following constant perturbation amplitudes A : 0.1, 0.6, 0.8, 0.95 and 1.4. It is an appropriate choice to obtain a fairly good overview of the system behaviour. Indeed, these values include the optimal amplitudes A^* which were introduced in the previous subsection in table 2 to maximize the perception of the images when the normalized spatial frequency was set to $N_{HF}/N^2 = 1/4$. To complete the general set-up, the noise intensity σ of the noisy image I_b at the input of the VR-detector is adjusted to the value which was used at the input of the SR-detector, namely $\sigma = 0.1$. It allows one to directly compare the performance between the two detectors in terms of image perception.

First, we analyse how the perturbation frequency influences the perception of the Saturn image through the VR-detector. For each value of the perturbation amplitude, the cross-covariance has been computed versus the normalized perturbation frequency N_{HF}/N^2 . For the sake of clarity, our results are presented in figure 12a where we have used a \log_2 scale for the horizontal axis.

We remark that the curve plotted with circles and which has been obtained with the perturbation amplitude $A = 0.95$ always remains beyond the other curves. It means that for this amplitude of the perturbation, the detector provides the best performance whatever the frequency of the perturbation. Of course, this specific value of the perturbation amplitude also corresponds to the optimal value A^* which was introduced in the previous section in table 2 to optimize the VR-detector versus the amplitude at constant frequency. Moreover, for the perturbation amplitudes below A^* , namely $A = 0.8$ (squares), $A = 0.6$ (crosses) and $A = 0.1$ (diamonds), the corresponding cross-covariance curves are ranked one on top of the other from the weakest amplitude A to the greatest one. By contrast, when the perturbation amplitude is set to $A = 1.4$ and exceeds A^* , the cross-covariance curve plotted with stars is always below the curve obtained with the optimal setting $A = A^*$. This specific behaviour indicates that irrespective of the perturbation frequency, the evolution of the cross-covariance versus the perturbation amplitude A follows the typical bell-shaped curves presented in the previous section and which constitutes the signature of VR.

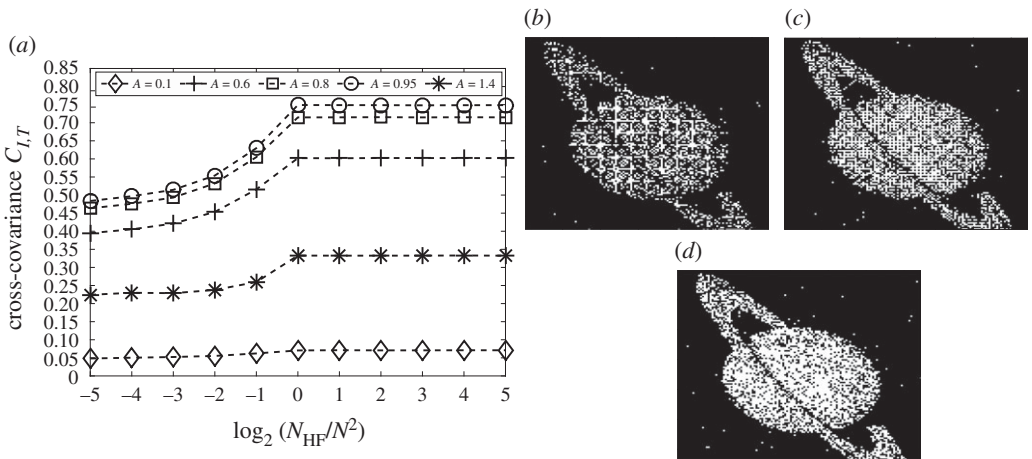


Figure 12. Effect of the perturbation frequency on the perception of Saturn through the VR-detector. Parameters: $N^2 = 2^{14}$, $V_{th} = 1.2$ and $\sigma = 0.1$. (a) Cross-covariance $C_{I,T}$ against the normalized perturbation frequency N_{HF}/N^2 for different amplitudes A of the perturbation. Dashed lines are guides to the eye. For the optimal perturbation amplitude $A^* = 0.95$, we have displayed the images perceived through the detector for three specific frequencies in subfigures (b–d). (b) $N_{HF} = 2^{13}$. (c) $N_{HF} = 2^{14}$. (d) $N_{HF} = 2^{15}$. The best perception of the Saturn image is achieved when the cross-covariance saturates to $C_{I,T} = 0.749$, that is when the perturbation is tuned to the optimal amplitude $A^* = 0.95$ and when its frequency is greater than the optimal value $N_{HF}^* = N^2 = 2^{14}$.

On the other hand, the perturbation frequency directly impacts the quality of the perceived image since all cross-covariance curves share the same feature: whatever the considered amplitude A of the perturbation, the cross-covariance monotonously grows with the frequency until it saturates to a maximum value reached for the optimal normalized frequency $N_{HF}^*/N^2 = 1$. The perturbation frequency N_{HF} is then optimally set to $N_{HF}^* = N^2$, which corresponds to the value of the image resolution. Note that when the perturbation frequency N_{HF} exceeds this optimal frequency N_{HF}^* , the wavelength of the perturbation becomes shorter than the interpixel distance leading to the saturation of the cross-covariance. In summary, the best perception of the Saturn image is achieved when the perturbation amplitude A matches $A^* = 0.95$ and when the perturbation frequency exceeds $N_{HF}^* = N^2 = 2^{14}$. Indeed, if we visually analyse the images obtained for the optimal amplitude $A^* = 0.95$, and presented for various frequencies in figure 12b–d, there is no doubt that tuning the detector with the optimal frequency N_{HF}^* better enhances the image perception. Moreover, for the other frequencies chosen below the optimal value N_{HF}^* in figure 12b,c, we can note that the information can also be perceived. However, as observed for the weakest frequency in figure 12b, the perturbation also dominates the threshold crossing events and induces the loss of some image details.

Next, we have performed the test bench of our VR-detector by using the other images. The frequency analysis is reported in figure 13 for the image of the Coloseum whose resolution is the weakest, namely $N^2 = 64^2$ pixels. To comment on the results, it is necessary to recall that in the previous section, we have established the exact value of the optimal perturbation amplitude A^* that maximizes the cross-covariance at constant frequency. This value, $A^* = 0.6$, is one of the considered amplitudes used to plot the cross-covariance versus the perturbation frequency in figure 13a. This curve, plotted with crosses, is always over the others indicating that the amplitude A^* maximizes the image perception independently from the considered frequency. Moreover, the curves obtained for the amplitude exceeding A^* , namely $A = 0.8$, $A = 0.95$ and $A = 1.4$, are located underneath each other and arranged from the weakest amplitude to the others. It shows that VR occurs whatever the frequency, with a more or less pronounced resonance, which is defined by the curve corresponding to the optimal amplitude $A^* = 0.6$ in figure 13a. In the case of the Coloseum

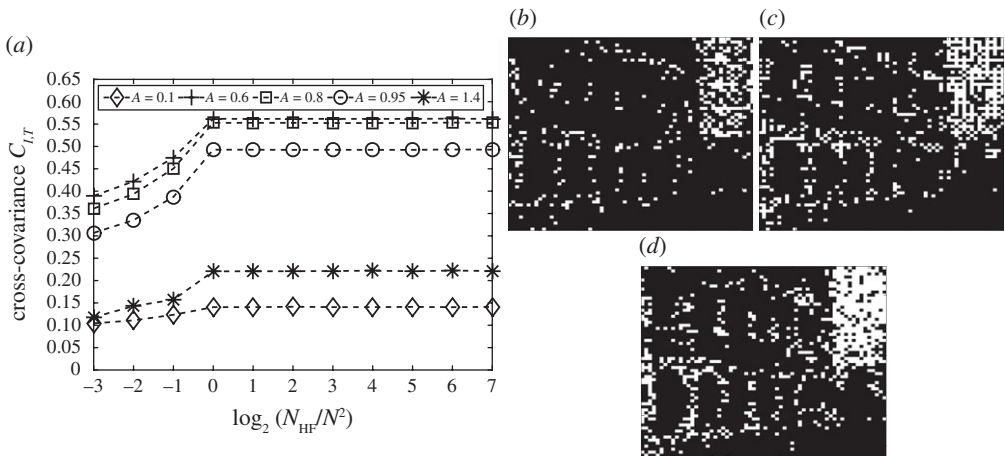


Figure 13. Effect of the perturbation frequency on the perception of the Coloseum through the VR-detector. Parameters: $N^2 = 2^{12}$, $V_{th} = 1.2$ and $\sigma = 0.1$. (a) Cross-covariance $C_{I,T}$ against the normalized perturbation frequency N_{HF}/N^2 for different amplitudes A of the perturbation. Dashed lines are guides to the eye. For the optimal perturbation amplitude $A^* = 0.6$, we have displayed the images perceived through the detector for three specific frequencies in subfigures (b–d). (b) $N_{HF} = 2^9$. (c) $N_{HF} = 2^{11}$. (d) $N_{HF} = 2^{12}$. The best perception of the Coloseum image is achieved when the cross-covariance saturates to $C_{I,T} = 0.562$, that is when the perturbation is tuned to the optimal amplitude $A^* = 0.6$ and when its frequency is greater than the optimal value $N_{HF}^* = N^2 = 2^{12}$.

image, the cross-covariance saturation occurs for all perturbation amplitudes, when the frequency N_{HF} exceeds the optimal value $N_{HF}^* = 2^{12}$, which exactly matches the image resolution $N^2 = 2^{12}$ pixels. Therefore, as visually presented in figure 13b–d for different perturbation frequencies, the best quality of perception is achieved when the perturbation of the VR-detector is optimally tuned with the amplitude $A^* = 0.6$ and the frequency $N_{HF}^* = 2^{12}$.

Lastly, for the images of the Cameraman and Lena, which are displayed in figures 14 and 15, the cross-covariance follows the same trend and, therefore, do not alter the conclusion previously drawn from the images of Saturn and the Coloseum. Indeed, in the case of the Cameraman picture with resolution $N^2 = 2^{16}$ pixels, the cross-covariance saturates for the optimal frequency $N_{HF}^* = 2^{16}$ whatever the perturbation amplitude. Similarly, for the Lena image of resolution $N^2 = 2^{18}$ pixels, the saturation of the cross-covariance appears at frequencies $N_{HF}^* = 2^{18}$. Moreover, for both images, the cross-covariance obtained for the optimal amplitude A^* always remains the greatest irrespective of the perturbation frequency. Therefore, the existence of the classical VR phenomenon for all the considered frequencies is clearly established whatever the considered image. Lastly, as shown by the images presented for various perturbation frequencies in figures 14b–d and 15b–d, to obtain the best perception enhancement of subthreshold images, it is confirmed that the perturbation must be adjusted with the optimal amplitude A^* and the optimal frequency $N_{HF}^* = N^2$. Indeed, the more the frequency is far from the optimal value $N_{HF}^* = N^2$, the more the crossing threshold events are governed by the perturbation rather than the subthreshold image. It involves a qualitative loss of the image details when the frequency is too weak compared to the optimal value $N_{HF}^* = N^2$. Lastly, we quantitatively compare in table 3 the performances of the VR-detector and SR-detector. The cross-covariance is given for the SR-detector tuned with its optimal noise level γ^* and for the optimally tuned VR-detector with optimal perturbation amplitude A^* and optimal frequency N_{HF}^* . We have also added the cross-covariance of the VR-detector whose perturbation frequency obeys to $N_{HF} = N^2/4$ and whose amplitude is optimally set to A^* .

Whatever the image and its resolution, the VR-detector clearly outperforms the SR-detector even if the perturbation frequency is not optimally tuned to N_{HF}^* but to $N_{HF} = N^2/4$.

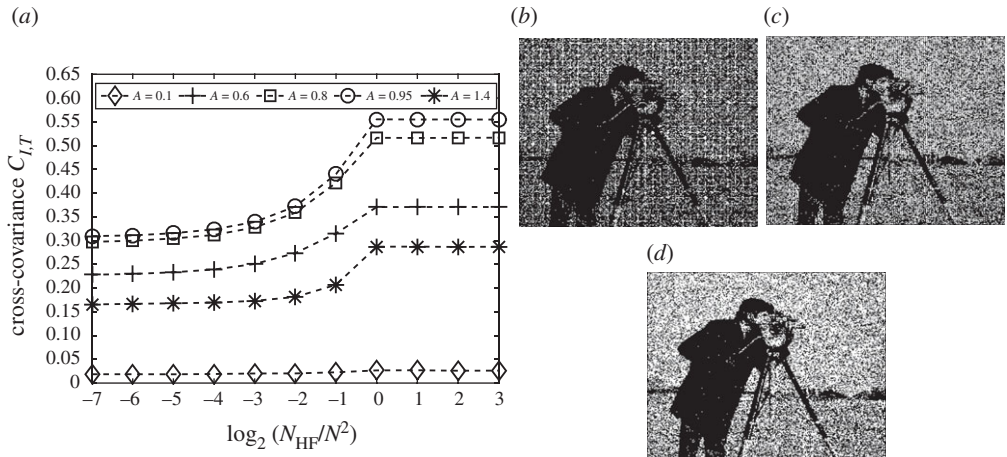


Figure 14. Effect of the perturbation frequency on the perception of the Cameraman through the VR-detector. Parameters: $N^2 = 2^{16}$, $V_{th} = 1.2$ and $\sigma = 0.1$. (a) Cross-covariance $C_{I,T}$ against the normalized perturbation frequency N_{HF}/N^2 for different amplitudes A of the perturbation. Dashed lines are guides to the eye. For the optimal perturbation amplitude $A^* = 0.95$, we have displayed the images perceived through the detector for three specific frequencies in subfigures (b–d). (b) $N_{HF} = 2^{13}$. (c) $N_{HF} = 2^{15}$. (d) $N_{HF} = 2^{16}$. The best perception of the Cameraman image is achieved when the cross-covariance saturates to $C_{I,T} = 0.565$, that is when the perturbation is tuned to the optimal amplitude $A^* = 0.95$ and when its frequency is greater than the optimal value $N_{HF}^* = N^2 = 2^{16}$.

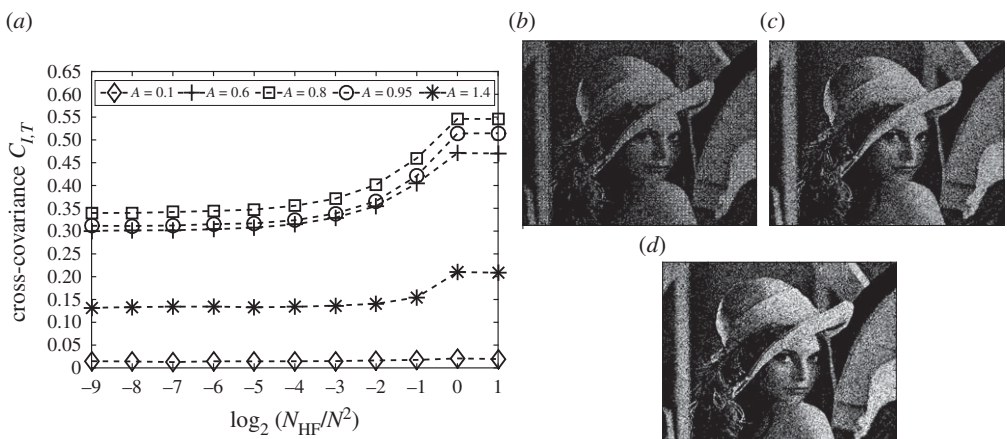


Figure 15. Effect of the perturbation frequency on the perception of Lena through the VR-detector. Parameters: $N^2 = 2^{18}$, $V_{th} = 1.2$ and $\sigma = 0.1$. (a) Cross-covariance $C_{I,T}$ against the normalized perturbation frequency N_{HF}/N^2 for different amplitudes A of the perturbation. Dashed lines are guides to the eye. For the optimal perturbation amplitude $A^* = 0.8$, we have displayed the images perceived through the detector for three specific frequencies in subfigures (b–d). (b) $N_{HF} = 2^{15}$. (c) $N_{HF} = 2^{17}$. (d) $N_{HF} = 2^{18}$. The best perception of the Lena image is achieved when the cross-covariance saturates to $C_{I,T} = 0.546$, that is when the perturbation is tuned to the optimal amplitude $A^* = 0.8$ and when its frequency is greater than the optimal value $N_{HF}^* = N^2 = 2^{18}$.

6. Conclusion

In this paper, we have first reviewed some applications of nonlinear resonances in the context of image processing and visual perception. Next, we have focused our study on the perception

Table 3. Features of the VR- and SR-detectors when the noise level of the input subthreshold image is $\sigma = 0.1$ and when the detector threshold is $V_{\text{th}} = 1.2$.

| image number and size N^2 | best cross-covariance of VR-detector with $N_{\text{HF}} = N^2/4$ $C_{I,T}(A^*, N_{\text{HF}} = N^2/4)$ | best cross-covariance of VR-detector $C_{I,T}(A^*, N_{\text{HF}}^*)$ | best cross-covariance of SR-detector $C_{I,T}(\gamma^*)$ |
|--------------------------------|---|--|--|
| 1: Coloseum $N^2 = 2^{12}$ | 0.422 for $A^* = 0.6$ and $N_{\text{HF}} = 2^{10}$ | 0.562 for $A^* = 0.6$ and $N_{\text{HF}}^* = 2^{12}$ | 0.274 for $\gamma^* = 0.39$ |
| 2: Saturn $N^2 = 2^{14}$ | 0.554 for $A^* = 0.95$ and $N_{\text{HF}} = 2^{12}$ | 0.749 for $A^* = 0.95$ and $N_{\text{HF}}^* = 2^{14}$ | 0.322 for $\gamma^* = 0.5$ |
| 3: Cameraman $N^2 = 2^{16}$ | 0.372 for $A^* = 0.95$ and $N_{\text{HF}} = 2^{12}$ | 0.565 for $A^* = 0.95$ and $N_{\text{HF}}^* = 2^{16}$ | 0.199 for $\gamma^* = 0.59$ |
| 4: Lena $N^2 = 2^{18}$ | 0.401 for $A^* = 0.8$ and $N_{\text{HF}} = 2^{14}$ | 0.546 for $A^* = 0.8$ and $N_{\text{HF}}^* = 2^{18}$ | 0.208 for $\gamma^* = 0.465$ |

through a threshold detector of subthreshold noisy images which have different resolutions. The main feature of this detector is to use a perturbation whose parameters can be tuned to provide the best perception of the input subthreshold image whose noise level is σ . When the perturbation corresponds to noise, the well-known SR phenomenon takes place: there exists an optimal intensity of noise γ^* which optimizes the perception of the information contained in the noisy subthreshold input image. Indeed, using the cross-covariance $C_{I,T}$ as a measure of the similarity between the initial image I and the perceived image T , we have determined this optimal level of noise γ^* . We have shown that this specific noise value also corresponds to the critical noise intensity of the input image beyond which a spatial HF perturbation fails to retrieve the information of the subthreshold image. However, for images with a noise level below the critical value γ^* , considering a HF perturbation instead of noise gives rise to the VR phenomenon: similar to SR, there exists an appropriate setting of the perturbation parameters which provides the best perception of the subthreshold image. We have first characterized this VR-detector at constant frequency versus the amplitude of the perturbation to highlight that an optimal amplitude A^* of the perturbation maximizes the cross-covariance. It has led to a better enhancement of the visual perception through the detector than with the SR-detector. Next, we have analysed the impact of the spatial frequency N_{HF} of the perturbation when its amplitude A remains constant. It has been established that whatever the perturbation frequency N_{HF} , the amplitude which provides the best visual perception through the detector is always the same, namely A^* . Therefore, we have set the perturbation amplitude to this optimal value and considered different spatial frequencies of the perturbation. By considering different input subthreshold images with different sizes N^2 , we have established that the cross-correlation coefficient $C_{I,T}$, which quantizes the quality of the perceived image, saturates when the frequency exceeds the image resolution, namely N^2 . Therefore, we have clearly established that the VR detector must be tuned with a perturbation of optimal amplitude A^* and spatial frequency N_{HF} greater than the image resolution N^2 . Using this optimal setting, the VR-detector clearly outperforms the SR-detector provided that the noise of the input images is below γ^* .

In our work, we have restricted our study to spatial perturbations. It could be also interesting to consider spatio-temporal perturbations, i.e. perturbations which also evolve versus time. Indeed, as reviewed in the case of SR, such spatio-temporal perturbations have revealed a rich variety of applications in perceptual decision-making [49–51] and have also accounted for the process of perception by the retina [48]. More generally, as reported in the case of our detector, we trust that VR-based strategies could provide better results in various fields where SR is used. Lastly, this work might constitute a starting point for further investigations of more complex detectors which could induce applications in the area of image processing.

Data accessibility. This article has no additional data.

Authors' contributions. All authors participated in the writing of the manuscript. All authors read and approved the manuscript.

Competing interests. We declare we have no competing interests.

Funding. No funding has been received for this article.

References

- Rajasekar S, Sanjuán MAF. 2016 *Nonlinear resonances*. Springer Series on Synergetics. Cham, Switzerland: Springer.
- Pikovsky A, Kurths J. 1997 Coherence resonance in a noise-driven excitable system. *Phys. Rev. Lett.* **78**, 775–778. ([doi:10.1103/PhysRevLett.78.775](https://doi.org/10.1103/PhysRevLett.78.775))
- Lindner B, Schimansky-Geier L. 2000 Coherence and stochastic resonance in a two-state system. *Phys. Rev. E* **61**, 6103. ([doi:10.1103/PhysRevE.61.6103](https://doi.org/10.1103/PhysRevE.61.6103))
- Lasserre G, Morfu S, Marquié P. 2009 Coherence resonance in a Bonhoeffer-Van der Pol circuit. *Electron. Lett.* **45**, 669–670. ([doi:10.1049/el.2009.0544](https://doi.org/10.1049/el.2009.0544))
- Gammaitoni L, Hänggi P, Jung P, Marchesoni F. 1998 Stochastic resonance. *Rev. Mod. Phys.* **70**, 223–287. ([doi:10.1103/RevModPhys.70.223](https://doi.org/10.1103/RevModPhys.70.223))
- Simonotto E, Riani M, Seife C, Roberts M, Twitty J, Moss F. 1997 Visual perception of stochastic resonance. *Phys. Rev. Lett.* **78**, 1186–1189. ([doi:10.1103/PhysRevLett.78.1186](https://doi.org/10.1103/PhysRevLett.78.1186))
- Xu B, Duan F, Bao R, Li J. 2002 Stochastic resonance with tuning system parameters: the application of bistable systems in signal processing. *Chaos Solitons Fractals* **13**, 633–644. ([doi:10.1016/S0960-0779\(00\)00266-6](https://doi.org/10.1016/S0960-0779(00)00266-6))
- Duan F, Chapeau-Blondeau F, Abbott D. 2013 Weak signal detection: condition for noise-induced enhancement. *Dig. Sig. Proc.* **23**, 1585–1591. ([doi:10.1016/j.dsp.2013.05.009](https://doi.org/10.1016/j.dsp.2013.05.009))
- Zozor S, Amblard PO, Duchêne C. 2017 On pooling networks and fluctuation in suboptimal detection framework. *Fluct. Noise Lett.* **7**, L39–L60. ([doi:10.1142/S0219477507003684](https://doi.org/10.1142/S0219477507003684))
- Mc Donnell M, Stocks NG, Pearce EM, Abbott D. 2008 *Stochastic Resonance: from suprathreshold stochastic resonance to stochastic signal quantization*. New York, NY: Cambridge University Press.
- Ye Q, Huang H, Zhang C. 2004 Image enhancement using stochastic resonance [sonar image processing applications]. In *Int. Conf. on Image Proc., Singapore. ICIP '04*, vol. 1, p. 263. Piscataway, NJ: IEEE.
- Histace A, Rousseau D. 2006 Constructive action of noise for impulsive noise removal in scalar images. *Electron. Lett.* **42**, 393–395. ([doi:10.1049/el:20060180](https://doi.org/10.1049/el:20060180))
- Histace A, Rousseau D. 2010 Noise-enhanced nonlinear PDE for edge restoration in scalar images. In *IEEE 2010 Int. Conf. on Soft Computing and Pattern Recognition*. Piscataway, NJ: IEEE. ([doi:10.1109/socpar.2010.5685935](https://doi.org/10.1109/socpar.2010.5685935))
- Landa P, McClintock PVE. 2000 Vibrational resonance. *J. Phys. A: Math. Gen.* **33**, L433–L438. ([doi:10.1088/0305-4470/33/45/103](https://doi.org/10.1088/0305-4470/33/45/103))
- Ullner E, Zaikin A, García-Ojalvo J, Báscones R, Kurths J. 2003 Vibrational resonance and vibrational propagation in excitable systems. *Phys. Lett. A* **312**, 348–354. ([doi:10.1016/S0375-9601\(03\)00681-9](https://doi.org/10.1016/S0375-9601(03)00681-9))
- Chizhevsky VN, Smeu E, Giacomelli G. 2003 Experimental evidence of 'Vibrational Resonance' in an optical system. *Phys. Rev. Lett.* **91**, 220602. ([doi:10.1103/PhysRevLett.91.220602](https://doi.org/10.1103/PhysRevLett.91.220602))
- Bordet M, Morfu S. 2012 Experimental and numerical enhancement of vibrational resonance in neural circuit. *Electron. Lett.* **48**, 903–905. ([doi:10.1049/el.2012.1343](https://doi.org/10.1049/el.2012.1343))
- Bordet M, Morfu S. 2013 Experimental and numerical study of noise effects in a FitzHugh-Nagumo system driven by a biharmonic signal. *Chaos Solitons Fractals* **54**, 82–89. ([doi:10.1016/j.chaos.2013.05.020](https://doi.org/10.1016/j.chaos.2013.05.020))
- Morfu S, Bordet M. 2018 On the correlation between phase-locking modes and vibrational resonance in a neuronal model. *Commun. Nonlinear Sci. Numer. Simul.* **55**, 277–286. ([doi:10.1016/j.cnsns.2017.07.023](https://doi.org/10.1016/j.cnsns.2017.07.023))
- Bordet M, Morfu S, Rossé M, Marquié P. 2015 Propagation enhancement in a neural network. *Electron. Lett.* **51**, 1482–1484. ([doi:10.1049/el.2015.2258](https://doi.org/10.1049/el.2015.2258))
- Morfu S, Bordet M. 2017 On the propagation of a low frequency excitation in a perturbed FitzHugh-Nagumo system: simulation and experiments. *Chaos Solitons Fractals* **103**, 205–212. ([doi:10.1016/j.chaos.2017.06.006](https://doi.org/10.1016/j.chaos.2017.06.006))

22. Hongler M, De Menes Y, Beyeler A, Jacquot J. 2003 The resonant retina: exploiting vibrational noise to optimally detect edges in an image. *IEEE Trans. Pattern Anal. Mach. Intell.* **25**, 1051–1062. (doi:10.1109/TPAMI.2003.1227982)
23. Chizhevsky VN, Giacomelli G. 2005 Improvement of signal to noise ratio in a bistable optical system: comparison between vibrational and stochastic resonance. *Phys. Rev. A* **71**, 011801. (doi:10.1103/PhysRevA.71.011801)
24. Chizhevsky VN, Giacomelli G. 2008 Vibrational resonance and the detection of aperiodic binary signals. *Phys. Rev. E* **77**, 051126. (doi:10.1103/PhysRevE.77.051126)
25. Chizhevsky VN. 2018 Amplification of an autodyne signal in a bistable vertical-cavity surface-emitting laser with the use of a vibrational resonance. *Tech. Phys. Lett.* **44**, 17–19. (doi:10.1134/S1063785018010066)
26. Ren Y, Pan Y, Duan F, Chapeau-Blondeau F, Abbott D. 2017 Exploiting vibrational resonance in weak-signal detection. *Phys. Rev. E* **96**, 022141. (doi:10.1103/PhysRevE.96.022141)
27. Ren Y, Pan Y, Duan F. 2018 Generalized energy detector for weak random signals via vibrational resonance. *Phys. Lett. A* **382**, 806–810. (doi:10.1016/j.physleta.2018.01.015)
28. Morfu S, Usama BI, Marquié P. 2019 Perception enhancement of subthreshold noisy image with vibrational resonance. *Electron. Lett.* **55**, 650–652. (doi:10.1049/el.2018.8059)
29. Xu B, Duan F, Bao R, Li J. 2002 Stochastic resonance with tuning system parameters: the application of bistable systems in signal processing. *Chaos Solitons Fractals* **13**, 633–644. (doi:10.1016/S0960-0779(00)00266-6)
30. Xu B, Duan F, Chapeau-Blondeau F. 2004 Comparison of aperiodic stochastic resonance in a bistable system realized by adding noise and by tuning system parameters. *Phys. Rev. E* **69**, 061110. (doi:10.1103/PhysRevE.69.061110)
31. Yang Y, Jiang Z, Xu B, Repperger DW. 2009 An investigation of two-dimensional parameter-induced stochastic resonance and applications in nonlinear image processing. *J. Phys. A: Math. Theor.* **42**, 145207. (doi:10.1088/1751-8113/42/14/145207)
32. Dylov DV, Fleischer JW. 2010 Nonlinear self-filtering of noisy images via dynamical stochastic resonance. *Nat. Photonics.* **4**, 323–328. (doi:10.1038/nphoton.2010.31)
33. Dylov DV, Waller L, Fleischer JW. 2012 Nonlinear restoration of diffused images via seeded instability. *IEEE J. Quantum. Electron.* **18**, 916–925. (doi:10.1109/JSTQE.2011.2159829)
34. Sun Q, Liu H, Huang N, Wang Z, Han J, Li S. 2015 Nonlinear restoration of pulse and high noisy images via stochastic resonance. *Sci. Rep.* **5**, 16183. (doi:10.1038/srep16183)
35. Feng X, Liu H, Huang N, Wang Z, Zhang Y. 2019 Reconstruction of noisy images via stochastic resonance in nematic liquid crystals. *Sci. Rep.* **9**, 3976. (doi:10.1038/s41598-019-40676-6)
36. Vaudelle F, Gazengel J, Rivoire G, Godivier X, Chapeau-Blondeau F. 1998 Stochastic resonance and noise-enhanced transmission of spatial signals in optics: the case of scattering. *J. Opt. Soc. Am. B* **15**, 2674–2680. (doi:10.1364/JOSAB.15.002674)
37. Ryu C, Kong SG, Kim H. 2011 Enhancement of feature extraction for low-quality fingerprint images using stochastic resonance. *Pattern Recognit. Lett.* **32**, 107–113. (doi:10.1016/j.patrec.2010.09.008)
38. Chouhan R, Jha RK, Biswas PK. 2013 Enhancement of dark and low-contrast images using dynamic stochastic resonance. *IET Image Proc.* **7**, 174–184. (doi:10.1049/iet-ipr.2012.0114)
39. Chouhan R, Biswas PK, Jha RK. 2015 Enhancement of low-contrast images by internal noise-induced Fourier coefficient rooting. *SIViP* **9**, 255–263. (doi:10.1007/s11760-015-0812-2)
40. Rallabandi VPS, Roy PK. 2010 Magnetic resonance image enhancement using stochastic resonance in Fourier domain. *Magn. Reson. Imaging* **28**, 1361–1373. (doi:10.1016/j.mri.2010.06.014)
41. Rallabandi VPS. 2008 Enhancement of ultrasound images using stochastic resonance based wavelet transform. *Comput. Med. Imaging Graph.* **32**, 316–320. (doi:10.1016/j.compmedimag.2008.02.001)
42. Perona P, Malik J. 1990 Scale space and edge detection using anisotropic diffusion. *IEEE Trans. Pattern Anal. Machine Intell.* **12**, 629–639. (doi:10.1109/34.56205)
43. Morfu S, Marquié P, Nofiele B, Ginhac D. 2008 Nonlinear systems for image processing. *Adv. Imag. Electron Phys.* **152**, 79–153. (doi:10.1016/S1076-5670(08)00603-4)
44. Histace A, Rousseau D. 2012 Useful Noise effect for nonlinear PDE based restoration of scalar images. *Int. J. Comput. Inf. Syst. Ind. Manage. Appl.* **4**, 411–419.
45. Piana M, Canfora M, Riani M. 2000 Role of noise in image processing by the human perceptive system. *Phys. Rev. E* **62**, 1104–1109. (doi:10.1103/PhysRevE.62.1104)

46. Ditzinger T, Stadler M, Strüber D, Kelso JAS. 2000 Noise improves three-dimensional perception: stochastic resonance and other impacts of noise to the perception of autostereograms. *Phys. Rev. E* **62**, 2566–2575. (doi:10.1103/PhysRevE.62.2566)
47. Hennig HM, Kerscher NJ, Funk K, Wörgötter F. 2002 Stochastic resonance in visual cortical neurons: does the eye-tremor actually improve visual acuity? *Neurocomputing* **44–46**, 115–120. (doi:10.1016/S0925-2312(02)00371-5)
48. Zozor S, Amblard PO, Duchêne C. 2009 Does eye tremor provide the hyperacuity phenomenon. *J. Stat. Mech.* **2009**, P01015. (doi:10.1088/1742-5468/2009/01/p01015)
49. Itzovitch E, Riani M, Sannita WG. 2017 Stochastic resonance improves vision in the severely impaired. *Sci. Rep.* **7**, 12840. (doi:10.1038/s41598-017-12906-2)
50. Van der Groen O, Wenderoth N. 2016 Transcranial random noise stimulation of visual cortex: stochastic resonance enhances central mechanisms of perception. *J. Neurosci.* **36**, 5289–5298. (doi:10.1523/JNEUROSCI.4519-15.2016)
51. Moret B, Camilleri R, Pavan A, Lo Giudice G, Veronese A, Rizzo R, Campana G. 2018 Differential effects of high-frequency transcranial random noise stimulation (hf-tRNS) on contrast sensitivity and visual acuity when combined with a short perceptual training in adults with amblyopia. *Neuropsychologia* **114**, 125–133. (doi:10.1016/j.neuropsychologia.2018.04.017)
52. Gammaconi L. 1995 Stochastic resonance and the dithering effect in threshold physical systems. *Phys. Rev. E* **52**, 4691–4698. (doi:10.1103/PhysRevE.52.4691)
53. Nam H, Woo Lee S. 2009 Dithering artefacts in liquid crystal displays and analytic solution to avoid them. *IEEE Trans. Consum. Electron.* **55**, 2211–2215. (doi:10.1109/TCE.2009.5373790)
54. Woo Lee S, Nam H. 2009 A new dithering algorithm for higher image quality of liquid crystal displays. *IEEE Trans. Consum. Electron.* **55**, 2134–2138. (doi:10.1109/TCE.2009.5373779)
55. Lippel B, Kurland M. 1971 The effect of dither on luminance quantization of pictures. *IEEE Trans. Commun. Technol.* **19**, 879–888. (doi:10.1109/TCOM.1971.1090773)
56. Rousseau D, Delahaies A, Chapeau-Blondeau F. 2010 Structural similarity measure to assess improvement by noise in nonlinear image transmission. *IEEE Sign. Proc. Lett.* **17**, 36–39. (doi:10.1109/LSP.2009.2031734)
57. Amblard PO, Michel OJJ, Morfu S. 2005 Revisiting the asymmetric binary channel: joint noise-enhanced detection and information transmission through threshold devices. *Noise Complex Syst. Stoch. Dyn. III, SPIE* **5845**, 50–60. (doi:10.1117/12.609436)
58. Bulsara A, Zador A. 1996 Threshold detection of wideband signals: a noise-induced maximum in the mutual information. *Phys. Rev. E* **54**, R2185–R2188. (doi:10.1103/PhysRevE.54.R2185)
59. Chapeau-Blondeau F. 1997 Noise-enhanced capacity via stochastic resonance in an asymmetric binary channel. *Phys. Rev. E* **55**, 2016–2019. (doi:10.1103/PhysRevE.55.2016)
60. Kish LB, Harmer GP, Abbott D. 2001 Information transfer rate of neurons: stochastic resonance of Shannon's information channel capacity. *Fluct. Noise Lett.* **1**, L13–L19. (doi:10.1142/S0219477501000093)
61. Yao C, Liu Y, Zhan M. 2011 Frequency resonance-enhanced vibrational resonance in bistable systems. *Phys. Rev. E* **83**, 061122. (doi:10.1103/PhysRevE.83.061122)